Porous double-shell CdS@C$_3$N$_4$ octahedron derived by *in situ* supramolecular self-assembly for enhanced photocatalytic activity

Peng Chen[a], Fan Liu[a], Hongzhi Ding[a], Sheng Chen[a], Lang Chen[a,*], You-Ji Li[b], Chak-Tong Au[c], Shuang-Feng Yin[a,*]

[a] *State Key Laboratory of Chemo/Biosensing and Chemometrics, Provincial Hunan Key Laboratory for Cost-effective Utilization of Fossil Fuel Aimed at Reducing Carbon-dioxide Emissions, College of Chemistry and Chemical Engineering, Hunan University, Changsha, 410082, Hunan, China*
[b] *Key Laboratory of Mineral Cleaner Production and Exploit of Green Functional Materials in Hunan Province, Jishou University, Jishou, 416000, Hunan, China*
[c] *College of Chemistry and Chemical Engineering, Hunan Institute of Engineering, Xiangtan, 411104, Hunan, China*

A B S T R A C T

Multi-component nanomaterials with intricate multishell architectures hold great potential for the development of advanced photocatalytic materials. However, most of the multishell hollow materials reported so far are single-component, and it is rare to come across multi-component ones with hybrid compositions. Herein, we demonstrate a facile *in situ* supramolecular self-assembly strategy to synthesize hollow, porous and double-shell octahedron of CdS@C$_3$N$_4$ composition. By virtue of compositional and structural advantages, the CdS@C$_3$N$_4$ composites exhibit outstanding activity and stability in photocatalytic H$_2$ generation and selective oxidation of saturated C—H bonds.

1. Introduction

Micro- or nano-sized materials with hollow and porous structures are large in surface-to-mass ratio, and high in loading capacity as well as surface exposure. With these characteristics, they could be used as catalysts and adsorbents [1]. It was demonstrated that for photo-catalytic interactions, materials of multi-shell structures are superior to those of conventional simple structures [2,3]. The phenomenon is at-tributed to the higher light absorption ability of the former as a result of multi-scattering and multi-reflection within the hollow and porous structures, as well as to the shortened charge-carrier-diffusion distances in the thin-shell topologies. Binary-oxide photocatalysts of multi-shell and hollow structures have been reported, such as multi-shell ZnO hollow microspheres [4], shell-in-shell TiO$_2$ hollow microspheres [5], and triple-shell CeO$_2$ hollow microspheres [6]. With the advances of synthetic approaches, considerable efforts have been devoted to the construction of hollow architectures, not only of simple but also of complex compositions. For example, there are reports on the synthesis of multi-shell Au/CeO$_2$, Au/Cu$_2$O and TiO$_2$/Fe$_2$TiO$_5$ hollow spheres [7–9]. It was reported that metal sulfides with multi-shell and hollow micro- or nano-structures are better in photocatalytic performance compared with their metal-oxide counterparts [10]. Box-in-box NiS, double-shell NiCo$_2$S$_4$ hollow spheres as well as multi-shell Cu$_2$S were fabricated by anionic exchange or hard-template method [11,12].

With suitable band-gap width (2.4 eV) and band-edge position, CdS is promising in visible-light-driven photocatalysis in areas such as pollutant degradation [13], hydrogen evolution [14] and organic synthesis [15,16]. Unfortunately, bulk CdS has major drawbacks. First, the use of visible light is not optimized and there is ready recombina-tion of electron-hole pairs [17–19]. Another fatal drawback is the self-oxidation of S^{2-} and the release of Cd^{2+} under the influence of pho-togenerated holes, and such instability restricts practical applications [20]. Therefore, great efforts have been made to fabricate CdS with exquisite nanostructures or constructed type-II heterostructures to en-hance photocatalytic performance as well as catalyst stability [19,21]. Exploiting the merits of heterojunction and hierarchical structure, Lou et al. synthesized multi-shell hollow ZnS/CdS cages *via* ion exchange using ZIF-8 as template [22]. In addition, a way to prevent photo-cor-rosion of chalcogenides is to fabricate a core-shell structure, where the protective shell passivates the surface trap states of core materials [20]. For example, carbon-based materials were used to protect CdS from photo-corrosion [23]. Among the carbon-based materials, polymeric graphitic carbon nitride (g-C$_3$N$_4$) has attracted much attention because of its abundance, thermal and chemical stability as well as visible-light responsiveness [24,25]. Coupling with C$_3$N$_4$ to form core-shell structure can not only enhance the photostablity but also the photocatalytic

---

activity of CdS [26]. There are reports on carbon nitride hetero-composites as well as on the modification of carbon nitride materials with simple architectures using supramolecular assembly methods [27–29]. Nevertheless, architectural g-C_3N_4 of diverse morphology such as helix, multi-shell microspheres and porous frameworks were rarely synthesized using direct approaches, but commonly by hard- or soft-templating methods [30,31]. To our awareness, it is a big challenge to directly couple metal sulfides with C_3N_4 for the generation of composites with multi-shell architectures.

Herein, we report the facile fabrication of double-shell CdS@C_3N_4 octahedron (denoted herein as 2-CSCN) by an *in situ* supramolecular self-assembly approach. We evaluated the photocatalytic performance of 2-CSCN for hydrogen production in water splitting as well as selective oxidation of saturated C−H bonds under visible light illumination. It was observed that 2-CSCN displays photocatalytic activity and stability superior to CdS and other CdS-C_3N_4 catalysts reported to date.

2. Experimental section

2.1. Synthesis of $Cd_3(C_3N_3S_3)_2$ micro-octahedral precursor (CdTMT)

All reagents were of analytical grade and used without further purification. $Cd_3(C_3N_3S_3)_2$ (CdTMT) micro-octahedral precursor was prepared following the precipitation method described elsewhere [32].

2.2. Synthesis of single-shell octahedral CdS-C_3N_4 composite (1-CSCN)

First, melamine (4 g) and NaOH (0.72 g) were dissolved in 80 mL of de-ionized water. Then CdTMT precursor (0.685 g) was added to the aqueous solution with stirring (30 min). The mixture was then transferred to a stainless steel autoclave and subject to hydrothermal treatment at 160 °C for 6 h. The precipitate was collected by filtration, washed with water and ethanol and dried at 80 °C overnight. The as-resulted powder was heated (5 °C min^{-1}) to 500 °C in a span of roughly 2 h under nitrogen to get 1-CSCN.

2.3. Synthesis of double-shell octahedral CdS-C_3N_4 composite (2-CSCN)

First, melamine (1 g) and NaOH (0.24 g) were dissolved in 80 mL of de-ionized water, followed by adding the prepared CdTMT precursor (0.685 g) with stirring (30 min). The mixture was then transferred to a stainless steel autoclave and subject to the first hydrothermal treatment at 160 °C for 2 h (to investigate the formation process, the intermediate was collected by centrifugation after cooling the solution to room temperature and is herein named as "Step-I"). Second, 1.5 g of melamine and 0.24 g of NaOH were dissolved in the above solution at room temperature. The mixture was then hydrothermally treated for a second time at 160 °C for another 2 h (the intermediate was also collected and named as "Step-II"). Then, the second step was repeated as a third hydrothermal treatment, and the produced yellow substance is named as "Step-III". Finally, the Step-III was heated to 500 °C at a heating rate of 5 °C min^{-1} and kept at this temperature for 2 h under nitrogen to get the 2-CSCN product.

2.4. Synthesis of CdS-C_3N_4 composite (CSCN)

First, melamine (4 g) was dissolved in 80 mL of de-ionized water. Then CdTMT precursor (0.685 g) was added to the aqueous solution with stirring (30 min). The mixture was then transferred to a stainless steel autoclave and subject to hydrothermal treatment at 160 °C for 6 h. The precipitate was collected by filtration, washed with water and ethanol, and dried at 80 °C overnight. The as-resulted powder was heated to 500 °C in a span of roughly 2 h under nitrogen (heating rate of 5 °C min^{-1}) to get CSCN.

2.5. Synthesis of mesoporous C_3N_4 (CN)

Briefly, 4 g of melamine was heated to 500 °C in a span of roughly 2 h under nitrogen (heating rate of 5 °C min^{-1}) to afford CN.

2.6. Synthesis of CdS

First, $Cd(NO_3)_2 \cdot 4H_2O$ (3.08 g) and $Na_2S \cdot 9H_2O$ (1.2 g) were separately dissolved in 40 mL of de-ionized water. Then the Na_2S aqueous solution was added to the $Cd(NO_3)_2$ aqueous solution with stirring (30 min). The mixture was then transferred to a stainless steel autoclave and subject to hydrothermal treatment at 160 °C for 6 h. The precipitate was collected by filtration, washed with water and ethanol, and dried at 80 °C overnight.

2.7. Catalyst characterizations

Powder X-ray diffraction (XRD) pattern was collected on a Bruker D8 Advance X-ray diffractometer with mono-chromatized Cu-Kα radiation (λ = 0.154 06 nm). The morphology and microscopic structure were observed over a field emission scanning electron microscope (FE-SEM, Hitachi S-4800) as well as a high-resolution transmission electron microscope (HR-TEM, JEM-2100F). X-ray photoelectron spectroscopy (XPS) was used to acquire the Cd 3d, S 2p, N 1s and C 1s spectra of samples with the binding energies (BE) calibrated against the C 1s peak (284.6 eV) of adventitious carbon, using Mg-Kα (hν = 1253.6 eV) as excitation source (XPS, SSX-100, Mg-Kα). The UV–vis diffuse reflectance spectra (UV–vis DRS) were recorded over a Cary-100 spectrophotometer, using $BaSO_4$ as background reference. The specific surface area of samples was studied by N_2 adsorption and desorption method at 77 K using a NOVA 1000e instrument (Quantachrome Instruments, USA), adopting the Brunauer-Emmet-Teller formula for calculation. The FTIR spectra were recorded with an IR Affinity-1 FTIR spectrometer (Shimadzu, Japan). Briefly, about 5.0 mg of each sample was added to 100 mg of KBr for pulverizing. Then, the FTIR spectra were recorded between 4000 and 400 cm^{-1} at scans of 4 cm^{-1} intervals.

Photocurrent was determined by an electrochemical analyser (CHI660E, Shanghai Chenhua electrochemical workstation) in a standard three-compartment cell containing 100 mL of 0.2 M Na_2SO_4 solution. In the analyzer, the as-prepared samples coated on the indium-tin oxide glass (2.0 cm × 2.0 cm) were used as working electrode (WE), a Pt minigrid as counter electrode (CE), and a saturated calomel electrode (SCE) as reference electrode. The distance between WE and CE was 0.3 cm during the measurement of photocurrent. At an applied potential of 0.1 V *versus* SCE, photocurrents of the samples were obtained under visible light using a Xe lamp (PerfectLight, PLS-SXE300D) provided with a 400 nm cutoff filter. Photoelectrochemical activity measurements were recorded employing an electrochemical analyser (CHI660E, Shanghai Chenhua electrochemical workstation) over a standard three-electrode system using the to-be-measured sample as working electrode, a Pt wire as counter electrode, and a saturated calomel electrode (SCE) as reference electrode. Mott-Schottky experiments were performed in a sodium sulphate electrolyte solution (0.2 M) (pH = 6.8), and the perturbation signals were 10 mV at a frequency of 1 kHz.

2.8. Photocatalytic hydrogen production

The photocatalytic hydrogen evolution experiments were performed in a 250 mL sealed quartz flask at a constant temperature of 5–8 °C and negative pressure. A 300 W xenon arc lamp (PerfectLight PLS-SXE300C, Beijing, China) with a cut-off filter of λ > 400 nm was used as light source to trigger the photocatalytic reaction. The lamp was positioned 5 cm away from the reactor, and the focused intensity on the flask was *ca.* 134 mW cm^{-2}. In a typical experiment, the photocatalyst (20 mg)

was dispersed in an aqueous solution of 20 vol% lactic acid (50 mL). Pt cocatalyst (1 wt%) was photo deposited on the catalysts by directly dissolving H_2PtCl_6 into the reactant suspension. Hydrogen was analyzed by a gas chromatograph (Agilent, 7820 A) equipped with a thermal conductive detector (TCD) using argon as carrier.

The apparent quantum yield (AQY) upon monochromatic 420 nm irradiation was measured as described in our previous works [21].

2.9. Photocatalytic oxidation of saturated C−H bonds

The reactions were carried out in a three-necked round-bottom flask fixed with a reflux condenser. In a typical experiment, 10 mmol of toluene together with 100 mg of catalyst were added into the flask, and oxygen ($2 \, mL \, min^{-1}$) was introduced to the bottom of the reaction mixture. Prior to visible-light irradiation, the mixture was magnetically stirred in the dark for 30 min to establish adsorption–desorption equilibrium. After a designated time of irradiation (PerfectLight PLS-SXE300C, Beijing, China), the oxygen flow was stopped and the catalyst was recovered by means of centrifugation. The products were identified using a Shimadzu GCMS-QP2010 ultra mass spectrometer and quantified over a GC 2010 Plus chromatograph equipped with a FID and a wax capillary column (30 m × 0.25 mm × 0.25 μm). The conversion of alkylarenes and yield of ketones or aldehydes were estimated by means of gas chromatography (GC 2010 Plus) using the internal standard method (decane as internal standard).

3. Results and discussion

The overall scheme of our strategy is illustrated in Fig. 1. In the hydrothermal treatment process, partial decomposition of octahedral $Cd_3(C_3N_3S_3)_2$ (denoted herein as CdTMT) happens and there is the release of CdS, cyanuric acid (CA), and sulfur (Fig. 1A) [33]. At the same time, there is hydrogen bonding between melamine and the released CA, resulting in the generation of CAM [34–39]. Simultaneously, the CdS crystal nuclei formed in hydrothermal treatment are surrounded by CAM entities to form complexes (denoted as CCAM). The resulted CCAM adsorbed on the surface of CdTMT composes a core-shell structure, establishing the polyhedron shape. The generation of 2-CSCN and 1-CSCN was achieved after polycondensation under calcination. As shown in Fig. 1B and b, the CdTMT octahedron precursor with smooth surface and 800–1000 nm in diameters were prepared according to our previous work [32]. After the first hydrothermal treatment but without calcination (Step-I), there is the formation of core-shell structure with rough surface as well as retention of octahedral morphology (Fig. 1C and c). In addition, there is a large cavity between the irregular solid core and octahedral shell. The presence of CdS, CA, melamine as well as CdTMT in Step-I was confirmed by XRD and FT-IR analysis (Fig. S1, Supporting information, SI). It should be noted that the decomposition rate of CdTMT and formation rate of CCAM can be controlled by regulating the reaction conditions. At optimized reaction time and temperature, there is facile supramolecular assembly of exogenous melamine with the *in situ* generated CA through hydrogen bonding on the surface of the remaining CdTMT, which results in a decrease of
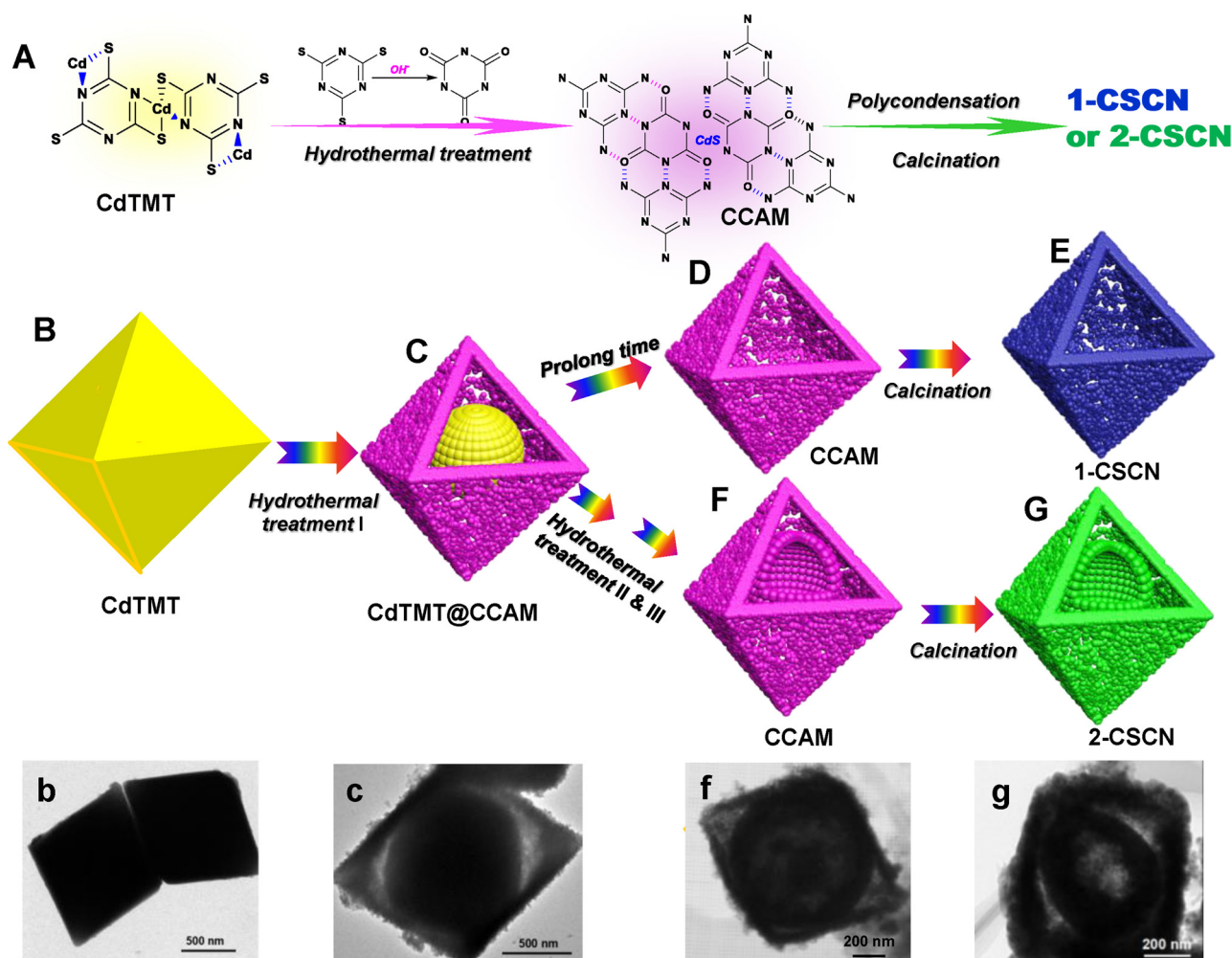

Fig. 1. Schematic of 2-CSCN synthesis.

melamine diffusion rate toward the inner core. When the supply rate of melamine is low, CdTMT@CCAM splits into inner and outer layers, forming a sort of irregular yolk-shell structure. The interior core is also irregular in shape. Therefore, we can obtain single-shell CdS-C_3N_4 hollow octahedron (1-CSCN) by prolonging the time of hydrothermal I (Fig. 1D and E). When the core-shell structure (Step-I) has undergone the second (Step-II) and third hydrothermal treatment (Step-III), there is the obvious appearance of a shell with a loose and hollow internal core, and finally double-shell octahedron (Fig. S2, SI). The composition of Step-III is mainly CCAM, and there is no detection of the characteristic CdTMT FT-IR peaks (Fig. S1, SI), which is in agreement with the proposed schematic (Fig. 1F and f). A process of temperature-programmed calcination was adopted to treat the resulted composite to afford the double-shell CdS-C_3N_4 octahedron (Fig. 1G and g), which has a composition of CdS and C_3N_4, and shows a phase structure similar to that of CSCN and 1-CSCN (Fig. S3, SI). Compared with the synthetic methods for multi-shell structures reported in the literature [40–42], the present strategy not only opens an avenue for the synthesis of double-shell CdS with hollow structures but also provides a way to manipulate shell composition.

As showed in Figs. 2A, B and S4 (SI), the 2-CSCN sample of octahedron appearance is porous and double-shell structured, with size mainly ranging from 800 to 1200 nm. The two shells are rough and made up of numerous nanoparticles. Between the outer and inner shell, there is the presence of gaps, and inside the core, a cavity. It is envisaged that the pores and gaps are beneficial for light scattering as well as reactant/product transfer. Unlike bulk samples, there is easy migration of photogenerated charges to the surfaces of 2-CSCN because of the thin shells (about 50 nm). In addition, the coupling of CdS particles with C_3N_4 (Fig. 2C) results in ample formation of heterojunctions, and according to EDS elemental mapping the distribution of C, N, Cd and S elements in 2-CSCN is uniform (Fig. 2D–G).

The composition and surface nature of 2-CSCN were analyzed by XPS and EDS. As shown in Fig. S5 (SI), there is the detection of Cd, S, N, C and O elements, and the high-resolution Cd 3d and S 2p spectra

confirm the presence of CdS [43]. The N 1s profile can be deconvoluted into three peaks: the one at 398.4 eV for sp^2-hybridized nitrogen in triazine rings (C−N═C), the one at 400.1 eV for tertiary nitrogen N−(C)3, and the one at 401.3 eV for C−N−H(2) (Fig. S5d) [44,45]. Overall, the XRD, XPS and EDS (Fig. S5f) results illustrate that the targeted CdS-C_3N_4 material has been successfully synthesized. Moreover, the specific surface area of 2-CSCN is (116.3 $m^2\,g^{-1}$) much larger than that of single-shell CdS-C_3N_4 octahedron (1-CSCN, 52.0 $m^2\,g^{-1}$) and CdS-C_3N_4 composite (CSCN, 7.3 $m^2\,g^{-1}$) (Tables S1, SI).

The effect of synthetic conditions on structural evolution was investigated. As revealed in SEM and TEM observations (Fig. S6, SI), the hydrothermal temperature plays a key role. The yolk-shell structure is generated at *ca.* 140 °C, whereas single-shell hollow structure at *ca.* 180 °C. However, in our previous work, under hydrothermal conditions CdTMT was found stable below 140 °C and the octahedral structure was found broken down into small particles at 160 °C [32]. These results suggest that a match of CdTMT decomposition rate and hydrogen bond formation rate is essential for the establishment of multi-shell structure. In Fig. S7 (SI), the yolk-shell structure is converted into hollow octahedron by prolonging hydrothermal treatment time, which is caused by a decrease of melamine diffusion rate toward the inner core. Taking hydrogen bonding (which acts as stabilizer for the octahedron structure) into account, we investigated the effect of NaOH amount on structure evolution (Fig. S8, SI). There is a breakdown of octahedral structure to small particles in the absence of NaOH. When NaOH content is low, the formed octahedrons are irregular in shape. In acidic or neutral situations, protons from water or acid would replace one or more of the cadmium atoms in CdTMT, forming trithiocyanuric acid as a result [33]. As a consequence, CA is not timely generated to maintain the octahedral structure. It is only when NaOH is in excess that there is acceleration of CdTMT decomposition, and the formation of yolk-shell hollow structure. It was found that the optimized condition for getting the double-shell composite with porous and hollow structure is: 160 °C for 2 h with 0.24 g of NaOH.

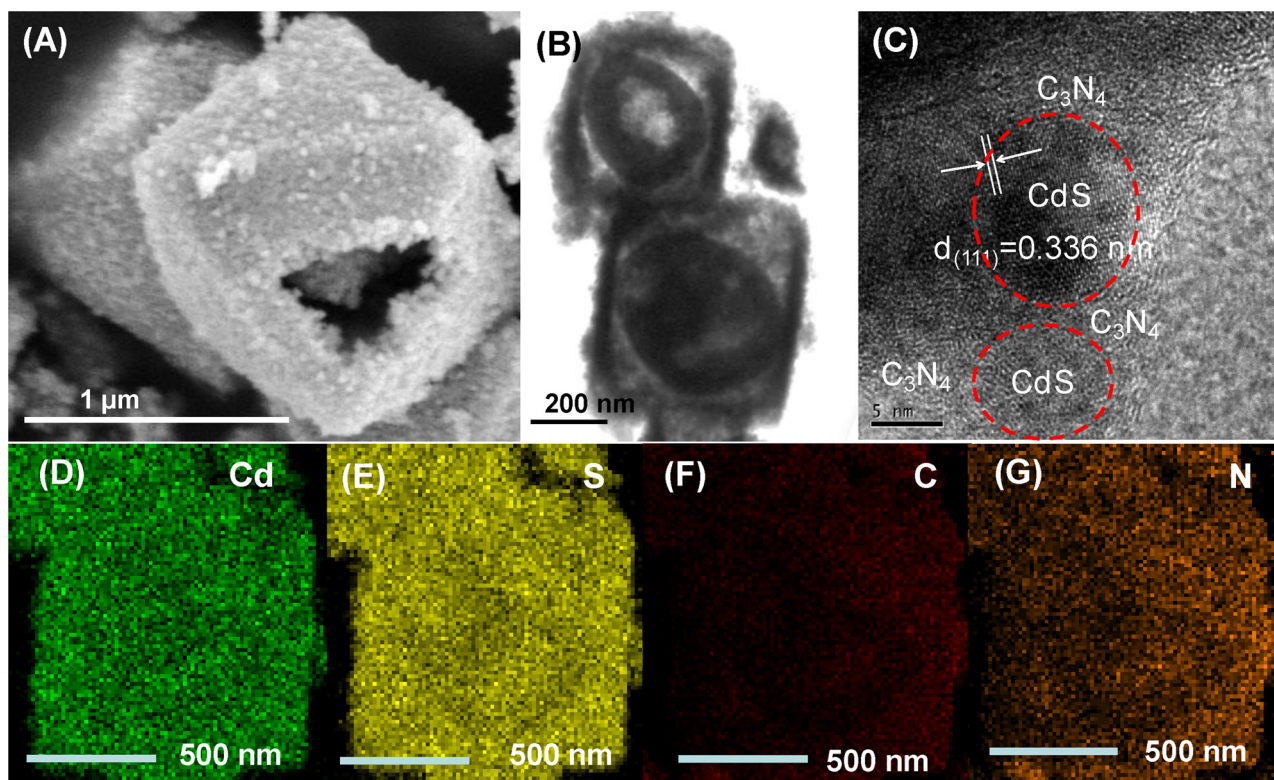We conducted UV–vis diffuse reflectance spectroscopic experiments

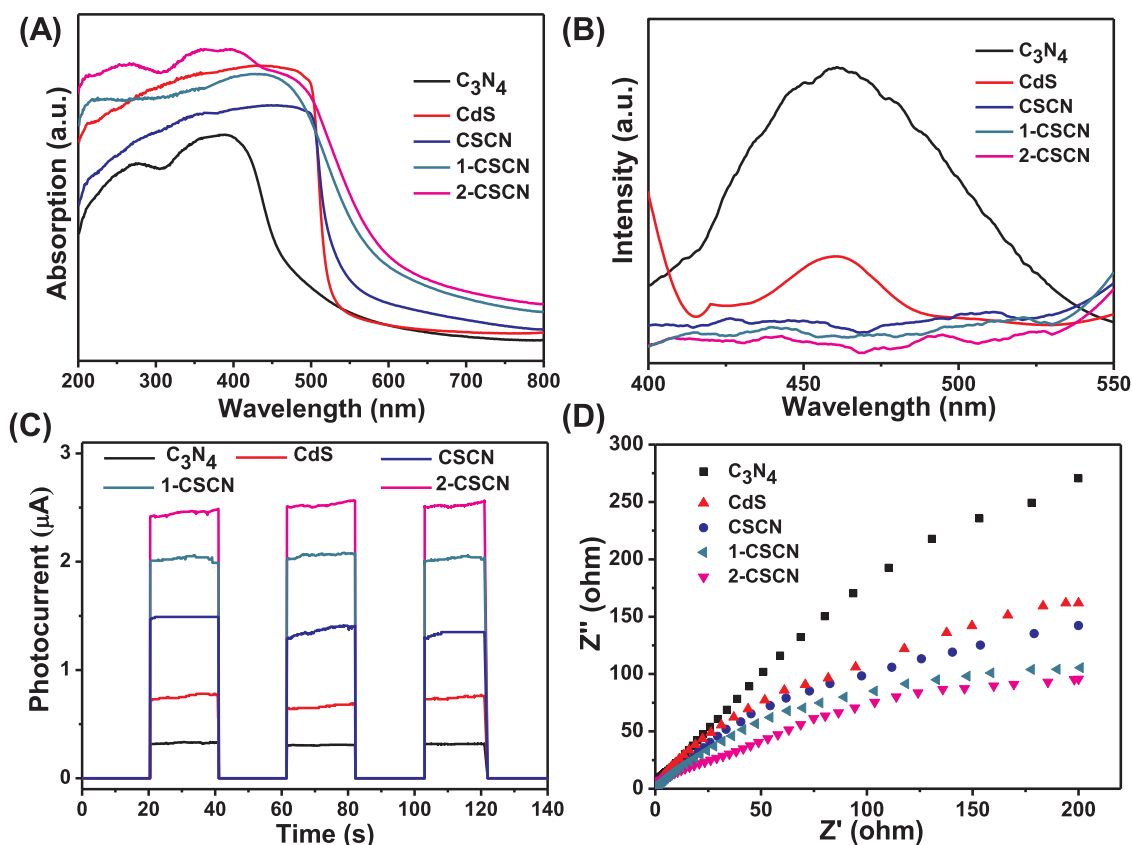**Fig. 2.** (A) SEM image, (B, C) TEM images and (D–G) elemental mapping images of 2-CSCN.

Fig. 3. (A) UV–vis DRS, (B) PL (λ_{Ex} = 350 nm), (C) photocurrent response and (D) electrochemical impedance spectroscopic spectra of fabricated samples.
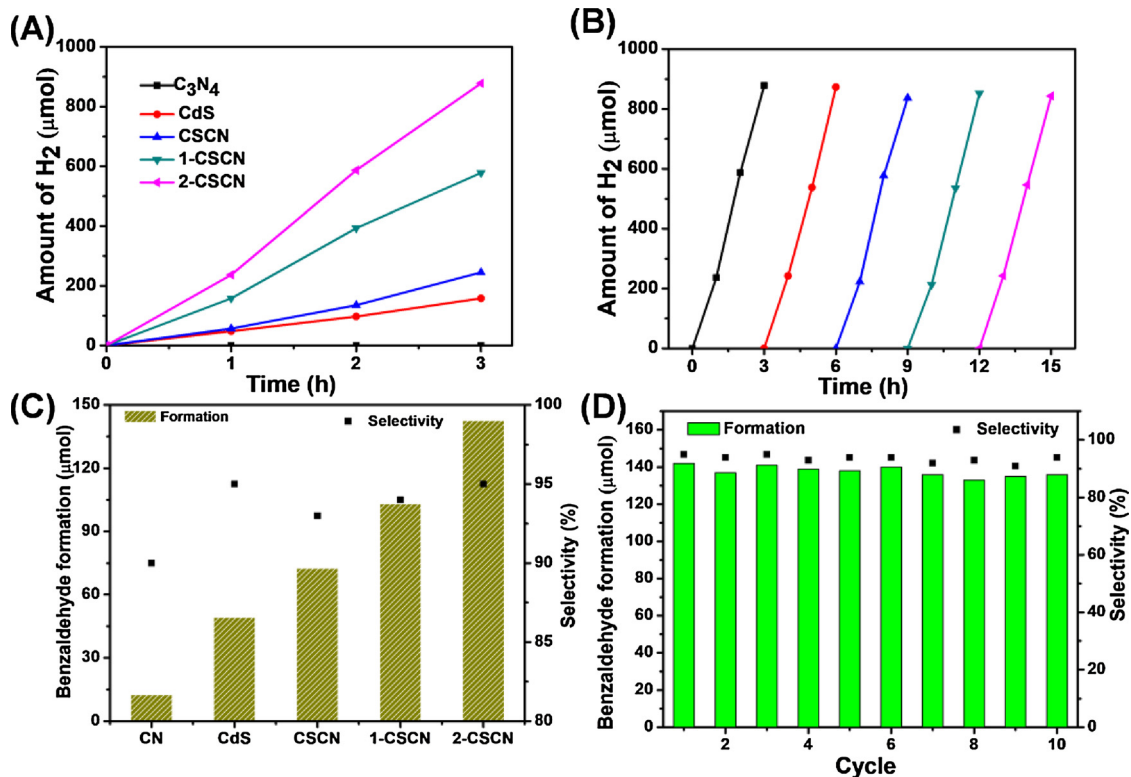

Fig. 4. (A) Time-dependent photocatalytic evolution of H_2 and (C) selective oxidation of toluene over CdS, C_3N_4, CSCN, 1-CSCN and 2-CSCN, cycling test of (B) photocatalytic H_2 evolution and (D) photocatalytic oxidation of toluene over 2-CSCN (Reaction conditions: photocatalyst 100 mg, substrate 10 mmol, no solvent, room temperature, O_2 flow rate 3 mL min^{-1}, visible-light irradiation λ > 400 nm, 3 h).
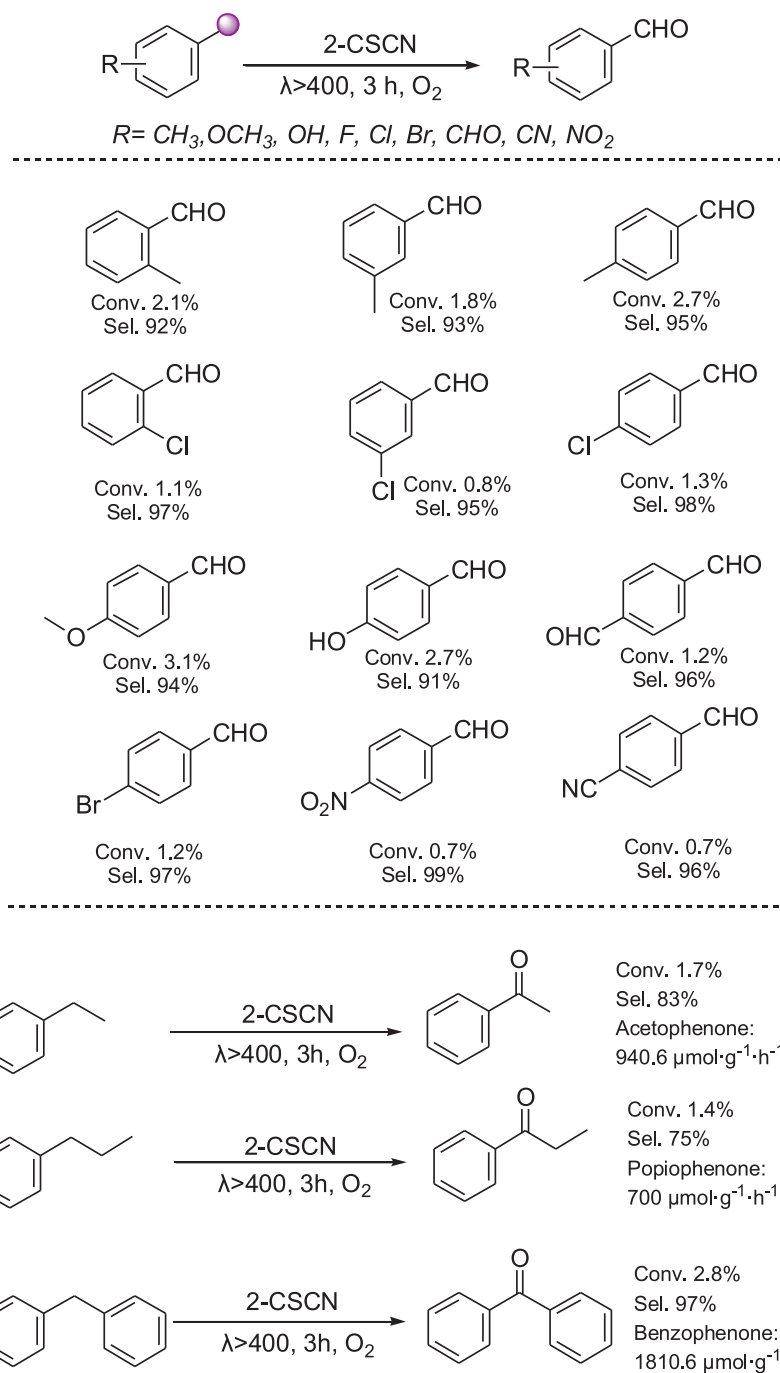
Fig. 5. Substrate scope for the photocatalytic oxidation of aromatic alkanes in this study. (Reaction conditions: photocatalyst 100 mg, substrate 10 mmol, no solvent, room temperature, O_2 flow rate 3 mL min^{-1}, visible light irradiation $\lambda > 400$ nm, 3 h).

to investigate the optical properties of the as-prepared samples. Bulk C_3N_4 (CN) exhibits an obvious absorption edge at *ca.* 450 nm, while 2-CSCN shows strong visible light absorption in the range of 400–700 nm (Fig. 3A). With the formation of the double shells, light harvesting capacity increases in both UV and visible light range. It is in agreement with the reported results that a multi-shell hollow structure with outer and inner shells is better than a single-shell one in light harvesting [46,47]. Meanwhile, the large specific surface area of the former not only facilitates light absorption but also enlarges the exposure of active sites for redox reactions. A combination of these positive effects would enable a porous multi-shell composite to perform well in photocatalytic reactions.

Room temperature photoluminescence (PL) as well as photo-

electron responses were carried out to investigate the separation efficiency of photogenerated charge carriers. As exhibited in Fig. 3B, the peak intensity of the samples are in the order of CN > CdS > CSCN > 1-CSCN > 2-CSCN. It is noted that the trend based on photocurrent intensity (*i.e.*, CN < CdS < CSCN < 1-CSCN < 2-CSCN) and that based on electrochemical impedance spectroscopic (EIS) investigations, (*i.e.*, CN > CdS > CSCN > 1-CSCN > 2-CSCN) is in harmony with the PL trend (Fig. 3C and D). On the basis of the PL, photocurrent intensity and EIS results, it is deduced that high light utilization (in consistence with the UV–vis absorption results) and excellent electron-transfer efficiency (type-II heterojunction was formed between CdS and C_3N_4) can be achieved over 2-CSCN.

The photocatalytic performance of the prepared samples were

evaluated for hydrogen production and selective oxidation of saturated C−H bonds under visible light irradiation. The average hydrogen evolution rate over C_3N_4, CdS, CSCN, 1-CSCN and 2-CSCN is *ca.* trace, 52.7, 81.7, 192.6 and 292.6 µmol h^{-1}, respectively (Fig. 4A). The 2-CSCN photocatalyst not only shows the highest activity among the as-prepared samples, but also the highest apparent quantum efficiency (420 nm) among the reported CdS-C_3N_4 composites at similar reaction conditions (Table S2, SI). The double-shell structure of the composites shows a great influence on photocatalytic activity. The apparent quantum yield (AQY) of 2-CSCN for hydrogen generation under monochromatic irradiation of 420 nm was calculated to be 17.2%. The excellent photocatalytic activity can also be ascribed to the rich presence of heterojunctions between CdS and C_3N_4 [48]. Besides, the thin shells endowed with abundant pores allow efficient charge transport across the surfaces, further inhibiting the recombination of charge carriers [20].

To investigate the stability of 2-CSCN, five consecutive cycles of the photocatalytic reaction were performed and each cycle lasted for 3 h (Fig. 4B). No apparent decrease of activity was detected, evidencing that the coating of C_3N_4 on CdS restrains photocorrosion. The schematic of energy level configuration and transfer process of photogenerated charge carriers is presented in Fig. S9 (SI). Under visible light, the unique mesoporous double shells and the cavities of 2-CSCN enables multiple reflections and scattering of light, thus enhancing light harvesting and offering more photogenerated electrons and holes [2,3]. Also, the hierarchical morphology of 2-CSCN facilitates the transfer of photogenerated electrons and holes. In detail, the photogenerated electrons on the LUMO level of C_3N_4 readily move into the conduction band of CdS, while the photogenerated holes on the valence band of CdS transfer to the HOMO of C_3N_4 [49]. In other words, there is enrichment of excited electrons in CdS and holes in C_3N_4. Meanwhile, the photogenerated holes on CdS rapidly migrate to C_3N_4 and thus substantially alleviates the problem of CdS photocorrosion [50]. At last, H_2O molecules undergo redox reactions at the catalytic centers, generating H_2 as a consequence.

The selective oxidation of saturated C−H bonds is one of the most fundamental processes in the synthesis of fine chemicals [51–53]. It has been demonstrated that at ambient conditions under visible light irradiation, heterogeneous photocatalysis proivdes a promising alternative for selective activation of C−H bonds [54]. In this study, the selective oxidation of toluene without solvent in the presence of O_2 and visible light was taken as model reaction. Under N_2 atmosphere or in the absence of a photocatalyst and/or light illumination, there is no detection of products, indicating the reaction is photocatalytic and O_2 (a green oxidant) is indispensable. It was observed that among the synthesized catalysts, 2-CSCN performs the best, showing benzaldehyde production rate of 475 µmol g^{-1} h^{-1} at a selectivity of up to 95% (Fig. 4C). Only a small amount of benzyl alcohol and no further oxidation products such as CO and CO_2 are detected. It was found that the approach is also effective for the selective oxidation of toluene derivatives (Fig. 5). It is noted that the oxidation of ethylbenzene or *n*-propylbenzene produces ketones rather than aldehydes, indicating only the alpha carbon of C−H bond is activated in this photocatalytic system. As revealed in Figs. 4D and S10 (SI), the loss of photoactivity across a test of 10 runs is insignificant, indicating high stability of 2-CSCN. Based on the results of scavenger experiments (Fig. S11 and discussions, SI), a possible reaction mechanism for partial oxidation of toluene over 2-CSCN is proposed and illustrated (Fig. S12, SI). The direct oxidation of toluene for the formation of toluene cationic radicals as facilitated by the holes is a key step. This step involves the activation of saturated C−H bonds which is often regarded as the rate-determining step for the selective oxidation of alkanes. Meanwhile, the electrons react with adsorbed O_2 to give activated oxygen species that selectively oxidize the cationic radicals, leading to the formation of benzaldehyde [55,56].

4. Conclusions

In summary, novel porous and hollow CdS@C_3N_4 octahedrons with double shells were fabricated by an *in situ* supramolecular self-assembly method. The coupling of CdS with C_3N_4 prevents the self-photooxidation of CdS and thus results in high photocatalyst stability. Owing to the porous and hollow structure, there is enhanced light absorption. Endowed with thin shells and heterostructures beneficial for the transfer of photogenerated charges, the CdS@C_3N_4 materials show much higher photocatalytic activity than its individual components as well as the single-shell CdS@C_3N_4 counterpart. The present work sheds light on the feasibility of similar approaches for the synthesis of advanced nanostructures of composition complexity targeted for specific applications.

Acknowledgements

Appendix A. Supplementary data

Supplementary material related to this article can be found, in the online version, at doi:https://doi.org/10.1016/j.apcatb.2019.04.006.

References

[1] J. Wang, H. Tang, L. Zhang, H. Ren, R. Yu, Q. Jin, J. Qi, D. Mao, M. Yang, Y. Wang, P. Liu, Y. Zhang, Y. Wen, L. Gu, G. Ma, Z. Su, Z. Tang, H. Zhao, D. Wang, Nat. Energy 1 (2016) 16050.
[2] G. Prieto, H. Tuysuz, N. Duyckaerts, J. Knossalla, G.H. Wang, F. Schuth, Chem. Rev. 116 (2016) 14056–14119.
[3] J. Qi, X. Lai, J. Wang, H. Tang, H. Ren, Y. Yang, Q. Jin, L. Zhang, R. Yu, G. Ma, Z. Su, H. Zhao, D. Wang, Chem. Soc. Rev. 44 (2015) 6749–6773.
[4] Z. Dong, X. Lai, J.E. Halpert, N. Yang, L. Yi, J. Zhai, D. Wang, Z. Tang, L. Jiang, Adv. Mater. 24 (2012) 1046–1049.
[5] S.H. Hwang, J. Yun, J. Jang, Adv. Funct. Mater. 24 (2014) 7619–7626.
[6] J. Qi, K. Zhao, G. Li, Y. Gao, H. Zhao, R. Yu, Z. Tang, Nanoscale 6 (2016) 4072–4077.
[7] P.F. Xu, R.B. Yu, H. Ren, L. Zong, J. Chen, X. Xing, Chem. Sci. 5 (2014) 4221–4226.
[8] B. Wang, R. Li, Z. Zhang, W. Zhang, X. Yan, X. Wu, G. Cheng, R. Zheng, J. Mater. Chem. A 5 (2017) 14415–14421.
[9] M. Waqas, Y. Wei, D. Mao, J. Qi, Y. Yang, B. Wang, D. Wang, Nano Res. 10 (2017) 3920–3928.
[10] C. Zhang, H. Liu, W. Wang, H. Qian, S. Cheng, Y. Wang, Z. Zha, Y. Zhong, Y. Hu, Appl. Catal. B: Environ. 239 (2018) 309–316.
[11] X.Y. Yu, L. Yu, L. Shen, X. Song, H. Chen, X.W. Lou, Adv. Funct. Mater. 24 (2014) 7440–7446.
[12] J. Guo, X. Zhang, Y. Sun, X. Zhang, L. Tang, X. Zhang, J. Power Sources 355 (2017) 31–35.
[13] C. Zhang, Y. Lu, Q. Jiang, J. Hu, Nanotechnology 27 (2016) 355402.
[14] Q. Li, B. Guo, J. Yu, J. Ran, B. Zhang, H. Yan, J.R. Gong, J. Am. Chem. Soc. 133 (2011) 10878–10884.
[15] J. Chen, X. Wu, L. Yin, B. Li, X. Hong, Z. Fan, B. Chen, C. Xue, H. Zhang, Angew. Chem. Int. Ed. 127 (2015) 1226–1230.
[16] S. Xie, Z. Shen, J. Deng, P. Guo, Q. Zhang, H. Zhang, C. Ma, Z. Jiang, J. Cheng, D. Deng, Y. Wang, Nat. Commun. 9 (2018) 1181.
[17] H. Tada, T. Mitsui, T. Kiyonaga, T. Akita, K. Tanaka, Nat. Mater. 5 (2006) 782–786.
[18] J. He, L. Chen, Z.Q. Yi, D. Ding, C.T. Au, S.F. Yin, Catal. Commun. 99 (2017) 79–82.
[19] X. Wu, X. Fan, S. Xie, J. Lin, J. Cheng, Q. Zhang, L. Chen, Y. Wang, Nat. Catal. 1 (2018) 772–780.
[20] Y.P. Xie, Z.B. Yu, G. Liu, X.L. Ma, H.M. Cheng, Energy Environ. Sci. 7 (2014) 1895–1901.
[21] J. He, L. Chen, F. Wang, Y. Liu, P. Chen, C.T. Au, S.F. Yin, ChemSusChem 9 (2016) 624–630.
[22] P. Zhang, B.Y. Guan, L. Yu, X.W. Lou, Chemistry 4 (2018) 162–173.
[23] Y. Hu, X. Gao, L. Yu, Y. Wang, J. Ning, S. Xu, X.W. Lou, Angew. Chem. Int. Ed. 52 (2013) 5636–5639.
[24] Z. Xu, H. Li, Z. Wu, J. Sun, Z. Ying, J. Wu, N. Xu, J. Mater. Chem. C 4 (2016) 7501–7507.
[25] Y. Xu, Z.C. Fu, S. Cao, Y. Chen, W.F. Fu, Catal. Sci. Technol. 7 (2017) 587–595.
[26] X.Y. Yu, L. Yu, X.W. Lou, Adv. Energy Mater. 6 (2016) 1501333.
[27] Y. Zheng, Z. Yu, H. Ou, A.M. Asiri, Y. Chen, X. Wang, Adv. Funct. Mater. 28 (2018)

[28] J. Barrio, C. Gibaja, J. Tzadikov, M. Shalom, F. Zamora, Adv. Sustain. Syst. 3 (2019) 1800138.
[29] J. Fu, J. Yu, C. Jiang, B. Cheng, Adv. Energy Mater. 8 (2018) 1701503.
[30] Y. Zheng, L. Lin, X. Ye, F. Guo, X. Wang, Angew. Chem. Int. Ed. 53 (2014) 11926–11930.
[31] Z. Tong, D. Yang, Z. Li, Y. Nan, F. Ding, Y. Shen, Z. Jiang, ACS Nano 11 (2017) 1103–1112.
[32] J. He, L. Chen, D. Ding, Y.K. Yang, C.T. Au, S.F. Yin, Appl. Catal. B: Environ. 233 (2018) 243–249.
[33] M.M. Matlock, K.R. Henke, D.A. Atwood, D. Robertson, Water Res. 35 (2001) 3649–3655.
[34] S. Yagai, T. Nakajima, K. Kishikawa, S. Kohmoto, T. Karatsu, A. Kitamura, J. Am. Chem. Soc. 127 (2005) 11134–11139.
[35] A.G. Bielejewska, C.E. Marjo, L.J. Prins, P. Timmerman, F.D. Jong, D.N. Reinhoudt, J. Am. Chem. Soc. 123 (2001) 7518–7533.
[36] Y.S. Jun, E.Z. Lee, X. Wang, W.H. Hong, G.D. Stucky, A. Thomas, Adv. Funct. Mater. 23 (2013) 3661–3667.
[37] M. Shalom, M. Guttentag, C. Fettkenhauer, S. Inal, D. Neher, A. Llobet, M. Antonietti, Chem. Mater. 26 (2014) 5812–5818.
[38] S. Wan, M. Ou, Q. Zhong, S. Zhang, W. Cai, Adv. Opt. Mater. 5 (2017) 1700536.
[39] J. Barrio, M. Shalom, ChemCatChem 10 (2018) 5573–5586.
[40] X. Lai, J. Li, B.A. Korgel, Z. Dong, Z. Li, F. Su, J. Du, D. Wang, Angew. Chem. Int. Ed. 50 (2011) 2738–2741.
[41] G. Zhang, X.W. Lou, Angew. Chem. Int. Ed. 126 (2014) 9187–9190.
[42] D. Li, X. Zhao, R. Yu, B. Wang, H. Wang, D. Wang, Inorg. Chem. Front. 5 (2018) 535–540.
[43] X. Zong, H. Yan, G. Wu, G. Ma, F. Wen, L. Wang, C. Li, J. Am. Chem. Soc. 130 (2008) 7176–7177.
[44] S. Yang, Y. Gong, J. Zhang, L. Zhan, L. Ma, Z. Fang, R. Vajtai, X. Wang, P.M. Ajayan, Adv. Mater. 25 (2013) 2452–2456.
[45] S. Guo, Z. Deng, M. Li, B. Jiang, C. Tian, Q. Pan, H. Fu, Angew. Chem. Int. Ed. 55 (2016) 1830–1834.
[46] Y. Zhao, L. Jiang, Adv. Mater. 21 (2009) 3621–3638.
[47] F. Caruso, R.A. Caruso, H. Möhwald, Science 282 (1998) 1111–1114.
[48] C. Yin, L. Cui, T. Pu, X. Fang, H. Shi, S. Kang, X. Zhang, Appl. Surf. Sci. 456 (2018) 464–472.
[49] S.W. Cao, Y.P. Yuan, J. Fang, M.M. Shahjamali, F.Y.C. Boey, J. Barber, S.C. Joachim Loo, C. Xue, Int. J. Hydrogen Energy 38 (2013) 1258–1266.
[50] Y. Xu, Y. Chen, W.F. Fu, Appl. Catal. B: Environ. 236 (2018) 176–183.
[51] X.H. Li, J.S. Chen, X. Wang, J. Sun, M. Antonietti, J. Am. Chem. Soc. 133 (2011) 8074–8077.
[52] L. Xiao, Q. Zhang, P. Chen, L. Chen, F. Ding, J. Tang, Y.J. Li, C.T. Au, S.F. Yin, Appl. Catal. B: Enivron. 248 (2019) 380–387.
[53] K. Cai, S.Y. Lv, L.N. Song, L. Chen, J. He, P. Chen, C.T. Au, S.F. Yin, J. Solid State Chem. 269 (2019) 145–150.
[54] X. Lang, X. Chen, J. Zhao, Chem. Soc. Rev. 43 (2014) 473–486.
[55] L. Chen, J. Tang, L.N. Song, P. Chen, J. He, C.T. Au, S.F. Yin, Appl. Catal. B: Environ. 242 (2019) 379–388.
[56] L.N. Song, F. Ding, Y.K. Yang, D. Ding, L. Chen, C.T. Au, S.F. Yin, ACS Sustain. Chem. Eng. 6 (2018) 17044–17050.

1705407.